PHYSICAL REVIEW C **91**, 064616 (2015)

Complete characterization of the fission fragments produced in reactions induced by ^{208}Pb projectiles on proton at 500*A* MeV

J. L. Rodríguez-Sánchez,[1] J. Benlliure,[1,*] J. Taïeb,[2] H. Álvarez-Pol,[1] L. Audouin,[3] Y. Ayyad,[1,†] G. Bélier,[2] G. Boutoux,[2,‡] E. Casarejos,[4] A. Chatillon,[2] D. Cortina-Gil,[1] T. Gorbinet,[2] A. Heinz,[5] A. Kelić-Heil,[6] B. Laurent,[2] J.-F. Martin,[2] C. Paradela,[1,§] E. Pellereau,[2] B. Pietras,[1] D. Ramos,[1] C. Rodríguez-Tajes,[7] D. M. Rossi,[6,‖] H. Simon,[6] J. Vargas,[1] and B. Voss[6]

[1]*Universidad de Santiago de Compostela, E-15782 Santiago de Compostela, Spain*
[2]*CEA, DAM, DIF, F-91297 Arpajon, France*
[3]*Institut de Physique Nucléaire d'Orsay, F-91406 Orsay, France*
[4]*Universidad de Vigo, E-36200 Vigo, Spain*
[5]*Chalmers University of Technology, SE-412 96 Gothenburg, Sweden*
[6]*GSI-Helmholtzzentrum für Schwerionenforschung GmbH, D-64291 Darmstadt, Germany*
[7]*Grand Accélérateur National d'Ions Lourds, F-14076 Caen Cedex 05, France*

(Received 14 April 2015; published 25 June 2015)

The two fragments produced in fission reactions induced by ^{208}Pb projectiles impinging on a liquid hydrogen target at 500*A* MeV have been fully identified in coincidence. The experiment was performed at GSI Darmstadt, where the combined use of the inverse kinematics technique with an efficient detection setup permitted one to detect and to fully identify the fission fragments in a range from $Z = 27$ to $Z = 52$. The corresponding isotopic cross sections and velocities of the fission fragments were measured with high accuracy. The results are compared to state-of-the-art model calculations that reproduce the measured observables. Correlations between the two fragments were used to assess the role of charge polarization and the excitation energy gained by the nascent fragments using the neutron excess of the final fragments. The analysis of the average velocities of the fission fragments allowed us to parametrize the distance between the two fission fragments at scission as a function of the size of the fissioning system.

DOI: 10.1103/PhysRevC.91.064616 PACS number(s): 24.70.+s, 24.75.+i, 25.40.Sc, 25.85.Ge

I. INTRODUCTION

Spallation reactions have recently raised an intense research activity, justified by their many practical applications in different fields: neutron spallation sources [1,2], accelerator-driven systems for incineration of nuclear waste [3], and production of radioactive beams [4–6] are some examples. Traditionally, spallation reactions on protons hold also interest for astrophysics because it is the dominating reaction mechanism induced by cosmic rays in the interstellar medium [7]. Beyond that, this type of reaction turns out to be an ideal tool for investigating different deexcitation channels over a wide range of temperatures and fissilities, in particular fission.

Spallation-induced fission is particularly well suited to investigate the coupling between the collective and intrinsic excitations in nuclei because fissioning compound nuclei are produced with high excitation energies and low angular momenta [8], fulfilling favorable conditions to study the evolution of this process [9].

In recent decades, the investigation of some observables such as pre- and postscission neutron multiplicities [10], γ ray [11], and charged particles [12] confirmed that the dynamical evolution of the fissioning system cannot be explained in terms of the transition-state approach [13], suggesting the need for including dissipative effects. Recently, it was also established that dissipative effects can explain fusion-fission cross sections at low excitation energies [14]. Unfortunately, that description of fission fails at high excitation energies [15,16] where the lifetime of the fissioning compound nucleus is dominated by transient time effects. Evidence of transient time effects was recently found in proton- and deuterium-induced fission of subactinides and actinides [17,18] at high excitation energies, providing relevant information about the dynamical evolution of the fissioning system from the ground state to the saddle point. The dynamical evolution beyond the saddle point [10] would require the complete characterization of both fission fragments in mass and atomic number.

Unfortunately, information on full isotopic distributions of fission fragments is scarce. First experiments were performed at the mass spectrometer Lohengrin [19] at the Institut Laue-Langevin using thermal-neutron-induced reactions [20–25]. This technique only allowed the identification of the light fission fragments because the velocities of the heavy ones are too small to correlate any measurable energy loss with their atomic number. In some cases, some isotopic yields of the heavy fragments could be obtained with radio-chemical techniques [26,27] or β-delayed γ spectroscopy [28,29], but with limited precision.

In the late 1990s, different experiments were performed at GSI using the FRS spectrometer [30] to investigate spallation-induced fission in inverse kinematics, accelerating heavy

*j.benlliure@usc.es
†Present address: Research Center for Nuclear Physics, Osaka University, Ibaraki, Osaka 567-0047, Japan.
‡Present address: Université Bordeaux, F-33405 Talence, France.
§Present address: EC-JRC, Institute for Reference Materials and Measurements, Retieseweg 111, B-2440 Geel, Belgium.
‖Present address: National Superconducting Cyclotron Laboratory, Michigan State University, East Lansing, MI 48824-1321, USA.

projectiles that impinged on liquid targets of hydrogen and deuterium. In these experiments only one of the two fragments was detected and identified in mass and charge by the FRS, however, these measurements provided relevant information on the ground-to-saddle fission dynamics at high excitation energies [31–36]. This technique was improved using a novel setup to measure the atomic number of both fission fragments [37], while the FRS spectrometer [30] was used to produce and select secondary beams of fissile nuclei produced in fragmentation reactions of ^{238}U. This experiment allowed one to investigate the role of shell effects in the charge distributions of the final fission fragments by Coulomb excitation of the incoming projectiles [37–39]. Moreover, fission dynamics at high excitation energy was investigated by means of fragmentation-induced fission reactions. In particular, partial fission cross sections and the width of the charge distributions of the final fission fragments as a function of the atomic number of the fissioning system were used to assess the ground-to-saddle fission dynamics at high excitation energy [17,40].

Recently, new experiments at GANIL also took advantage of the inverse kinematics technique together with transfer- and fusion-induced fission reactions [41–43]. In these experiments transfer reactions were identified and reconstructed with an annular segmented silicon detector [43]. One of the fission fragments was identified in mass and atomic number using the spectrometer VAMOS [44], while the second fragment was only identified in atomic number by energy-loss measurements using an ionization chamber and silicon detectors. These experiments provided for the first time complete mass- and atomic-number distributions of the fission fragments and their corresponding kinematics for several actinides such as ^{240}Pu and ^{250}Cf [42].

To go a step further, an effort was made recently by the SOFIA collaboration at GSI [45,46] to overcome the restrictions of conventional fission experiments to obtain complete isotopic measurements of both fission fragments. The present work reports on the results of proton-induced fission of ^{208}Pb obtained with this novel experiment in inverse kinematics, where both fission fragments were simultaneously detected and identified in atomic and mass number. These data allow us to validate a previous controversial measurement of the isotopic distributions of the fission fragments produced in the same reaction using the FRS spectrometer at GSI [35]. Taking advantage of the new experimental capabilities, correlations between the two fission fragments are investigated using the neutron excess and the widths of the isotopic distributions of the final fragments. These correlations allow us to assess the role of charge polarization and the excitation energy gained by the nascent fragments. Moreover, we use the average fission velocities of the fragments to investigate the distance between the two fission fragments at scission as a function of the size of the fissioning system.

II. EXPERIMENT

The experiment was performed at the GSI facilities in Darmstadt (Germany), where the SIS18 synchrotron was used to accelerate ions of ^{208}Pb up to 500A MeV with an intensity around 10^5 ions/s. The primary beam was then guided to Cave C where fission reactions were induced in a cylindrical target filled with liquid hydrogen ($\sim$85 mg/cm^2) produced in a cryostat. The target was isolated by two windows consisting of aluminized-mylar foils with a thickness of 35 μm. Finally, a novel setup especially designed for the investigation of fission in inverse kinematics was used to separate fission from other reaction channels and to facilitate the identification of both fission fragments in atomic and mass number.

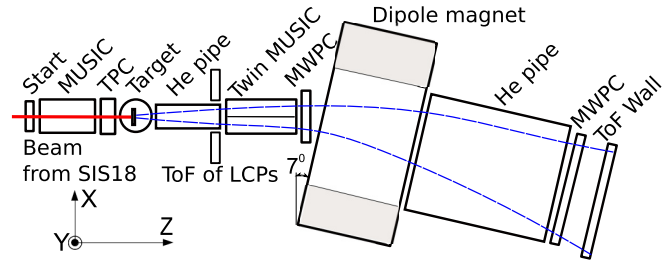

FIG. 1. (Color online) Top schematic view of the used experimental setup. Sizes are not to scale.

A. Description of the experimental setup

Figure 1 shows a top-view schematic representation of the detector setup [47,48] used in this experiment. The experimental setup is divided in two parts, one used to characterize the incoming beam ions and another dedicated to measure the fission fragments. The first part consists of a plastic scintillator detector (start) [49] used to measure the time of flight (ToF) of the fragments, a multisampling ionization chamber (MUSIC) [50], and a time projection chamber (TPC) [51]. These last two detectors provide the beam identification and its position on the target, respectively.

The second part consists of a double multisampling ionization chamber (twin MUSIC) [52], two multiwire proportional counters (MWPCs) [48,53], a large acceptance dipole magnet (ALADIN), and a ToF wall [49]. The twin MUSIC chamber, filled with P25 (74.5% of argon, 25% of CH_4, and 0.5% of CO_2) gas, has a central vertical cathode that divides its volume (60-cm long, 20-cm high, and 20-cm wide) into two active parts, segmented in 10 anodes each. These anodes provide 10 independent energy-loss and drift-time measurements, which allow one to obtain the atomic numbers with a resolution below 0.43 charge units full width at half maximum (FWHM) and the angles on the plane X-Z with a resolution below 0.6 mrad (FWHM). MWPCs, situated in front and behind the dipole magnet, provide the horizontal (X) and vertical (Y) positions of the fission fragments. The MWPC situated in front of the dipole magnet (20-cm high and 20-cm wide) provides the X and Y positions with a resolution around 200 μm and 1.5 mm (FWHM), respectively, while the MWPC situated behind the dipole magnet (60-cm high and 90-cm wide) provides those positions with a resolution around 300 μm and 2 mm (FWHM), respectively. Both MWPCs were filled with a mixture of argon (80%) and CO_2 (20%). Finally, a ToF wall (60-cm high and 90-cm wide) made of 28 plastic scintillators (3.2-cm wide, 60-cm long, and 0.5-cm thick) allows one to measure the ToF of the fission fragments with respect to the

start signal provided by the plastic scintillator located at the entrance of the experimental setup with a resolution around 40 ps (FWHM) [49]. The ALADIN magnet was set to a magnetic field of 1.6 T and its gap (200-cm long, 50-cm high, and 100-cm wide) was filled with helium gas at atmospheric pressure.

In addition, two pipes, also filled with helium gas at atmospheric pressure, were mounted in front of the twin MUSIC chamber and behind the dipole magnet ALADIN. The pipes were sealed by windows made of aluminized-mylar foils with a thickness of 35 μm and 50 μm, respectively. In all the cases, the helium gas was employed to reduce the energy and angular straggling of the fission fragments.

Finally, light-charged particles emitted in coincidence with fission fragments were identified using a ToF wall detector (ToF of LCPs), placed in front of the twin MUSIC chamber. This detector consists of two detection planes of segmented plastic scintillators (50-cm long, 6-cm wide, and 1-cm thick), one with six horizontal paddles and another with six vertical paddles, which leave a square hole (12.5×12.5 cm^2) in the center for the transmission of the fission fragments. The results obtained with this detector will be presented in a separate paper.

B. Identification of fission fragments

As discussed in Ref. [54], the ionization chamber MUSIC was used to select the beam projectiles with atomic number $Z = 82$, while the TPC chamber provided the position of the beam ions at the hydrogen target. Fission events were identified using the energy loss of the fragments in each part of the twin MUSIC chamber, and the tracking capabilities of this detector were used to select fission events produced at the target position.

The atomic number of the fission fragments could be deduced based on the fact that the energy loss is proportional to the atomic number squared. In Fig. 2(a) we show the measured atomic-number histogram in the left part of the twin MUSIC detector (dotted histogram), corrected by the corresponding ToF measurements as shown in Fig. 2(b). The final achieved resolution [solid histogram in Fig. 2(a)] was better than 0.43 charge units (FWHM). The peaks were then calibrated using a previous measurement of the isotopic distribution of the fission fragments produced in this reaction as a reference [35]. Similar results were obtained for the right part of the detector.

The sum of the atomic numbers of the two fission fragments corresponds to the atomic number of the fissioning system ($Z_1 + Z_2$) assuming no proton evaporation after scission. As shown in Ref. [57], the distribution obtained with the sum of the two atomic numbers provides an absolute calibration of the atomic number of the fissioning system. Taking this fact into account, in Fig. 3 we show a scatter plot of the atomic numbers registered in both sides of the twin MUSIC chamber after ToF corrections and based on independent calibrations. As can be seen in the figure, the dashed line corresponds to the atomic number $Z_1 + Z_2 = 83$, which is produced by single charge-exchange processes between projectile and target nuclei [55,56]. Beyond the dashed line one can also observe spots from the production of double charge-exchange reactions. These results are in agreement with previous measurements [57].

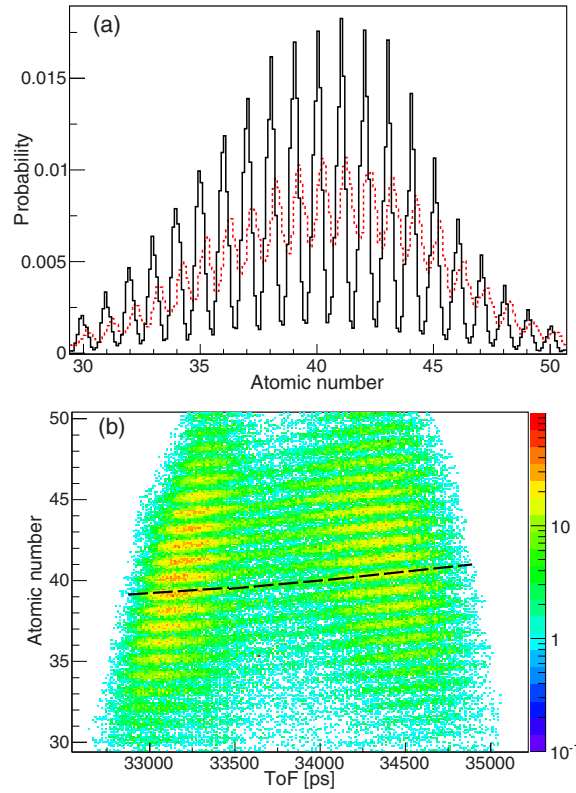

FIG. 2. (Color online) (a) Atomic-number histograms of fission fragments detected in the left part of the twin MUSIC chamber for the reaction ^{208}Pb (500A MeV) + p. The dotted histogram corresponds to the measured distribution, while the solid histogram represents the same distribution after ToF corrections. (b) Atomic number measured in the left side of the twin MUSIC detector as a function of the time of flight. The dashed line shows an example of the ToF correction needed to improve the resolution of the atomic number.

The horizontal positions obtained from the MWPCs and the angles from the twin MUSIC chamber give access to the curvatures of the trajectories of the fragments inside the dipole magnet ALADIN, providing their magnetic rigidity by taking into account the value of the magnetic field (1.6 T). The entrance angles on the plane X-Z were obtained from linear fits of the positions recorded by the 10 anodes of the twin MUSIC chamber. In Fig. 4 we present the position resolution (FWHM) of the anodes, obtained as the difference between the linear fit and the positions registered by the corresponding anode, as a function of the atomic number of the fission fragments. The position at each anode was obtained by using its drift-time signal and the velocity of the electrons in the gas. The resolution is shown for the left (solid squares) and right (solid circles) side. As can be seen in the figure, the resolution depends on the atomic number, as expected because the deposited energy in the anodes increases with the atomic number of the fission fragments. Therefore, the signal-to-noise ratio increases with the atomic number, improving the position resolution. In the figure, one can observe that both sections of the twin MUSIC chamber have similar position resolutions,

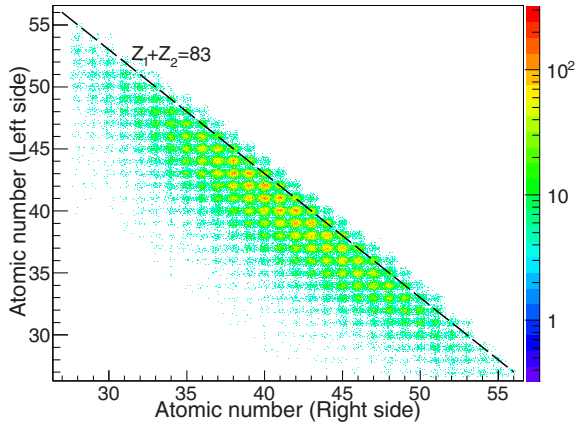

FIG. 3. (Color online) Atomic numbers registered in coincidence by the twin MUSIC in the reaction ^{208}Pb (500A MeV) + p. The dashed line represents the fissioning systems with atomic number $Z_1 + Z_2 = 83$.

evolving from 85 μm to 35 μm with the atomic number. These resolutions correspond to angular resolutions between 0.4 mrad and 0.1 mrad, respectively.

Full identification of the fission fragments is made using a ray-tracing method [58] coupled to GEANT4 simulations [59] to reconstruct their mass numbers. In the simulation, we took into account the composition, dimensions, and positions of the detectors, as well as the magnetic field and helium gas inside the dipole magnet ALADIN. Outside of the magnet we assume that fission fragments follow straight-line trajectories.

The reconstruction of the trajectories is performed using the measured atomic numbers, positions, and angles of the fission fragments before the dipole magnet ALADIN, as well as the positions on the target given by the TPC and tracking capabilities of the setup [54] as an input for the simulation. Then, different trajectories are simulated for each fission fragment covering the expected range of $B\rho$, between 6 and 10 Tm. The simulated trajectories are used to parametrize the flight path length and $B\rho$ of each fission fragment as a

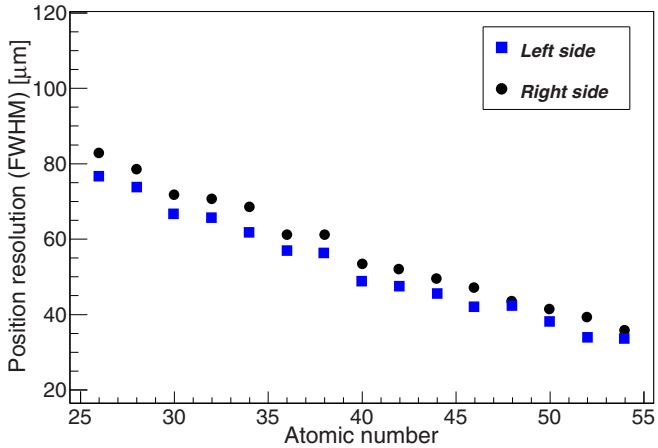

FIG. 4. (Color online) Mean position resolution provided by the twin MUSIC for the anodes used in the tracking as a function of the atomic number of the fission fragments.

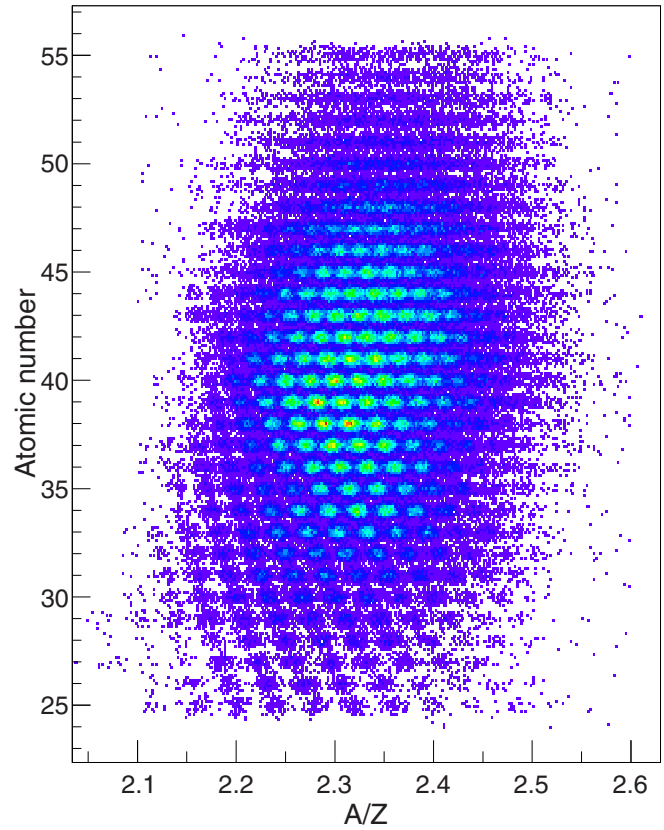

FIG. 5. (Color online) Cluster plot of the detected fission fragments displaying the correlations between the atomic number, obtained from energy loss measurements in the twin MUSIC detector, and the mass-over-charge ratio (A/Z) determined from magnetic rigidity and time-of-flight measurements. This plot provides a full and unambiguous identification in mass and atomic number of all fission fragments produced in the reaction ^{208}Pb (500A MeV) + p.

function of the position of the MWPC situated behind the dipole magnet. Then, this parametrization together with the experimental position recorded by the MWPC are used to obtain the experimental flight path length and $B\rho$ of each fission fragment. Finally, the measured ToF together with the reconstructed flight path length are used to deduce the velocity of the fragments with a resolution of $\Delta v/v \sim 0.11\%$ (FWHM).

Consequently, the mass number (A) is obtained for each fission fragment from its magnetic rigidity, velocity, and atomic number, according to the equation:

$$A = \frac{eZ}{u}\frac{B\rho}{\beta\gamma c}, \tag{1}$$

where Z is the atomic number provided by the twin MUSIC detector [see Fig. 2(a)], B is the magnetic field inside the magnet, ρ is the radius of the trajectory, u is the atomic mass unit, e is the electron charge, $\gamma = 1/\sqrt{1 - v^2/c^2}$, v is the velocity of the ion, and c is the velocity of light.

Using this procedure, the mass number of each fission fragment is obtained. The absolute calibration in mass number was obtained using previous measurements [35] as a reference. Figure 5 shows a scatter plot of the atomic number as a

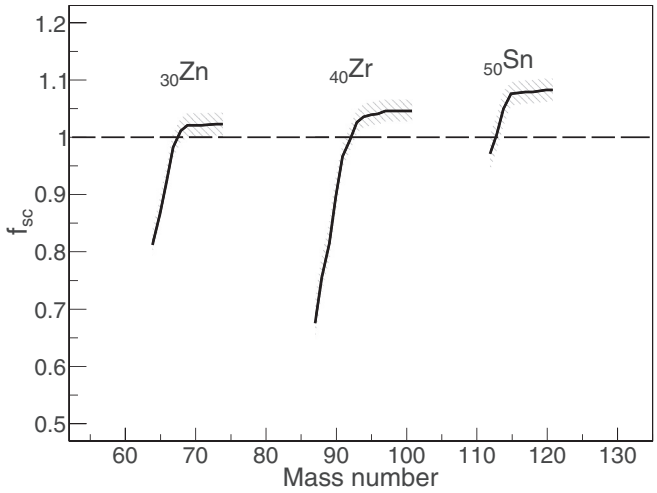

FIG. 6. Correction factor of secondary reactions (f_{sc}) is displayed for three elements ($_{30}$Zn, $_{40}$Zr, and $_{50}$Sn) as a function of the mass number.

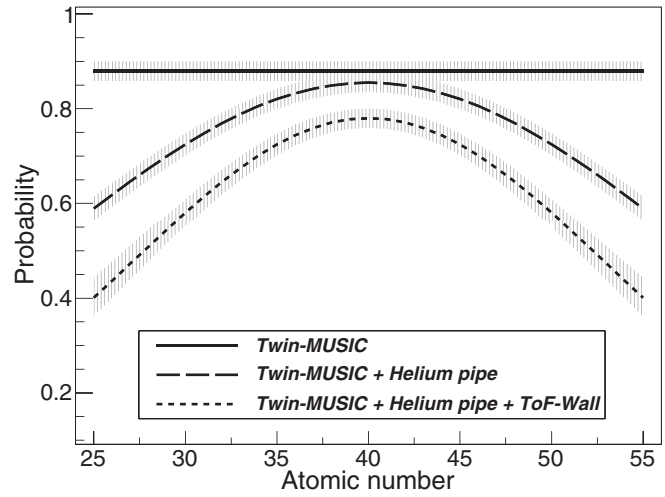

FIG. 7. Transmission as a function of the atomic number of the fission fragments. The lines represent the transmission corrections taking into account the geometrical constraints indicated in the figure.

function of the mass-over-charge ratio (A/Z) obtained in this experiment. As can be seen in the figure, a clear identification of fission fragments is achieved with an average resolution of $\Delta A/A \sim 0.63\%$ (FWHM).

C. Detection efficiency and transmission of fission fragments

In this section we will describe the corrections applied to the measured isotopic yields to account for the limited detection and geometrical efficiency of the experimental setup. The most important corrections are from secondary reactions, atomic charge states, and transmission of the fission fragments along the detection setup. The efficiency of the detectors for fission events was always above 98% with an uncertainty around 2%.

Secondary reactions in the experimental setup can be produced by two mechanisms: fission of an evaporation residue produced by a first spallation reaction or fragmentation of a fission fragment. In the first case, the probability of producing a fission event was estimated to be around 2.1% (see Ref. [54]) and its effect on the identification is negligible, however, the second mechanism is more important for an accurate identification. To describe the contribution to the measured yields from fragmentation reactions of fission fragments, the INCL4.6 [61] + ABLA07 [62] code was used. This code describes somewhat well the total reaction cross sections and the isotopic distributions of the residual fragments close in atomic and mass number to the projectile produced in spallation reactions [61]. Figure 6 shows this correction factor (f_{sc}) with its associated uncertainty (dashed area) for several elements as a function of the mass number of the fission fragments. As can be seen in the figure, the global effect of secondary reactions is to reduce the yields of neutron-rich fragments in favor of neutron-deficient ones. The main uncertainty of this correction factor comes from the total reaction cross sections calculated with the INCL4.6 model with an uncertainty around 5%.

The correction factor from atomic charge states (f_q) is needed for an accurate identification in the mass-over-charge ratio and was calculated along the setup by using the GLOBAL code [60]. This correction is negligible for nuclei with atomic numbers below 40 and increases exponentially up to 15% for $Z = 55$. The uncertainty of this correction varies from 4% to 1% for the atomic numbers $Z = 55$ and $Z = 40$, respectively.

Finally, the experimental setup used to measure the fission fragments has some geometrical constraints affecting the measured yields. These correction factors are obtained using GEANT4 simulations. The transmission corrections are calculated by counting the number of simulated fission fragments traversing the experimental setup with respect to the total number of simulated ones. In these calculations, only simulated fission events where both fission fragments are transmitted along the experimental setup were counted as fission events.

In Fig. 7 we show the different contributions with their associated uncertainties (dashed areas) to the correction accounting for the transmission of the fission fragments through the experimental setup. The solid line corresponds to the transmission correction factor from the dead zone produced by the central vertical cathode of the twin MUSIC chamber and to the probability that both fission fragments pass through the same part of this detector. The long-dashed line includes the previous correction but also the one from the limited size of the helium pipe situated in front of the twin MUSIC. Finally, the short-dashed line represents the transmission taking into account all geometric constraints along the setup, including the losses in the ToF wall. As can be seen in the figure, the transmission corrections are more important for lighter and heavier fragments because of the angular aperture of the lighter fragments.

Figure 8 shows the same corrections but in the form of isotopic distributions for three elements: $_{30}$Zn, $_{40}$Zr, and $_{50}$Sn. As can be seen in the figure, the evolution of the correction with the neutron excess is similar for the three elements although it is more important for the light fragments because of their larger angular apertures. The uncertainty of this correction is smaller than 5%.

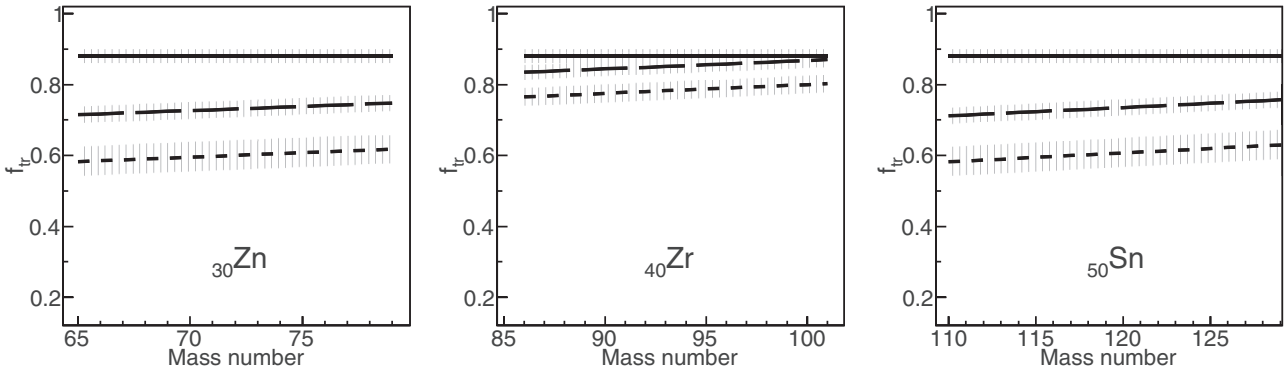

FIG. 8. Transmission coefficient (f_{tr}) as a function of the mass number for three elements: $_{30}$Zn (left), $_{40}$Zr (center), and $_{50}$Sn (right). The lines represent the transmission corrections taking into account the geometrical constraints indicated in Fig. 7.

III. RESULTS

In this section we present the results obtained in this work. We will mostly focus on the interpretation of the fragment properties produced on proton-induced fission of ^{208}Pb at 500A MeV. Observables such as velocities, isotopic cross sections, neutron excess, and the width of the isotopic distributions of the fission fragments are shown in comparison with previous measurements. In addition, mass and charge correlations between the two fragments are investigated as a function of the atomic numbers of the fission fragments. Our results are compared with calculations performed with the Liège intranuclear cascade code INCL4.6 [61] coupled to deexcitation code ABLA07 [62].

The code INCL4.6 [61] describes the first stage of the reaction between the proton and the lead nucleus as a series of independent nucleon-nucleon collisions, which leave an excited remnant nucleus at the end of the cascade. This nucleus usually deexcites by emitting particles or by fissioning. This last process is described by the deexcitation code ABLA07 [62] which uses the Weisskopf formalism [63] for the evaporation of particles ($Z < 3$), while the fission probability is determined by an analytical solution of the Fokker-Planck equation [17] that provides a time-dependent fission-decay width. The evaporation of intermediate-mass fragments (IMFs) is also implemented.

The description of the fission fragments properties is based on a semiempirical model [32]. In this work we will only comment on the most important features related to the super-long fission channel, which dominates at high excitation energies. This fission channel can be explained by the macroscopic properties of the potential-energy landscape that is determined by the characteristics of the fissioning nucleus at the saddle point. In particular, the stiffness of the macroscopic potential along the mass-asymmetry degree of freedom is obtained from the systematics of the width of mass distributions measured in Ref. [64]. The neutron-to-proton ratio (N/Z) of the fission fragments is assumed to be given by the unchanged-charge distribution (UCD). This N/Z is modified by the charge polarization effect calculated in terms of the liquid-drop model (LDM) assuming a two touching spheres configuration at the scission point [65], and by the evaporation of particles during the descent from saddle to scission [62]. Finally, at the scission point the two fission fragments are characterized by their atomic numbers $Z_{1,2}$, mass numbers $A_{1,2}$, kinetic energies $E^{1,2}_{\rm kin}$, and excitation energies $E^{1,2}_{x}$. After the formation of the two fission fragments, their corresponding deexcitation chains are followed until their excitation energies fall below the lowest particle-emission threshold.

A. Isotopic distributions of the fission fragments

The isotopic distributions of the fission fragments are one of the key observables for the understanding of the fission process and could provide valuable information about the excitation energy gained by the fissioning nucleus in the reaction as well as some of its properties at scission, such as polarization and shell effects [37–39,66–68].

To determine the isotopic distributions of the fission fragments, the measured isotopic yields were extracted from Fig. 5. The real production yields $Y(Z,A)$ were then obtained by correcting the measured yields $N(Z,A)$ by the factors accounting for the limitations of the experimental setup according to

$$Y(Z,A) = N(Z,A) f_{\rm sc} f_q / f_{\rm tr}, \qquad (2)$$

where $f_{\rm sc}$ is the correction factor from secondary reactions of the fission fragments, f_q is the correction of the atomic charge states, and $f_{\rm tr}$ is the detection efficiency of the setup (see Sec. II 3). Finally, the isotopic cross sections are obtained normalizing the isotopic yields to twice the total fission cross section measured in the present experiment [54].

In Fig. 9 we show the measured isotopic cross-section distributions of fission products (solid circles) for elements between cobalt ($Z = 27$) and tellurium ($Z = 52$). The values of the isotopic cross sections are also listed in the appendix. There was still some production by fission of fragments below cobalt and above tellurium, but these isotopic cross sections are not listed because the geometrical efficiency or mass resolution do not allow us to extract them with sufficient accuracy. The displayed measurement covers all the isotopes for each element with a statistical uncertainty below 10%. The complete isotopic production is compared with INCL4.6 [61] +ABLA07 [62] calculations (dashed lines). This comparison shows a very good agreement between our measurement and the calculations.

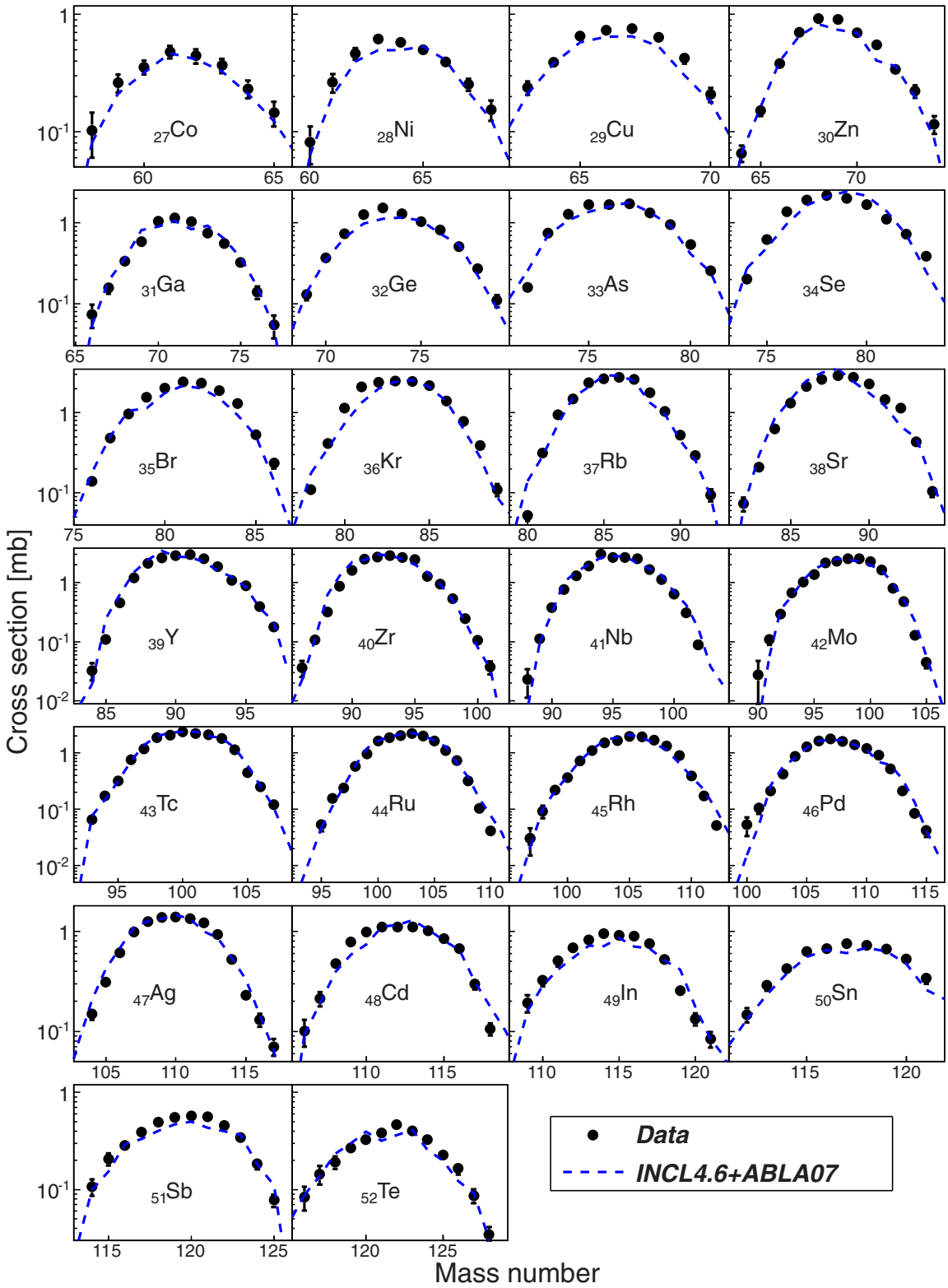

FIG. 9. (Color online) Isotopic cross sections measured in the reaction ^{208}Pb (500A MeV) + p corresponding to elements from cobalt to tellurium. Statistical uncertainty bars are shown if they exceed the size of the symbols. The dashed lines correspond to calculations.

The distributions in atomic and mass number of the fission fragments are shown in Figs. 10(a) and 10(b), respectively. Figure 10(a) shows the atomic-number distribution of the fission fragments measured in this work (solid circles) by adding the yields of the fragments with the same atomic number. These data are compared with the previous measurement by Fernández-Domínguez and collaborators (open circles) [35] performed with the FRS spectrometer at GSI.

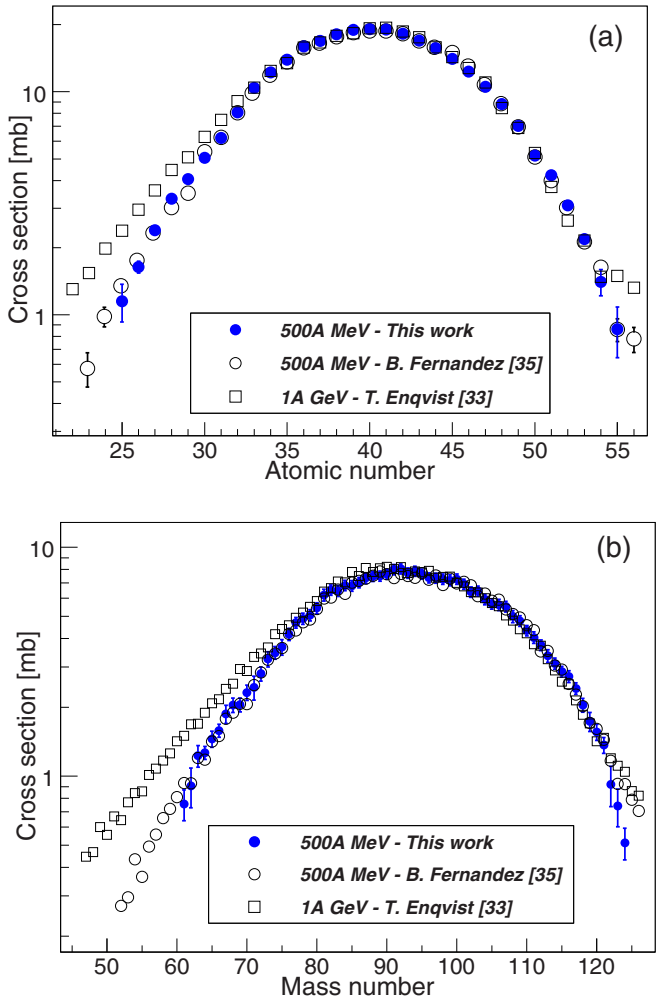

FIG. 10. (Color online) Cross sections of the final fission fragments. The solid circles and the open circles correspond to our new measurement and the data of Ref. [35] for the reaction ^{208}Pb (500A MeV) + p, respectively. The open squares correspond to the reaction ^{208}Pb (1A GeV) + p [33]. The uncertainties are shown if they exceed the size of the symbols. (a) As a function of the atomic number. (b) As a function of the mass number.

In Ref. [54], it was shown that the total fission cross section obtained at the FRS spectrometer (232 ± 33 mb) presents a significant deviation from recent measurements by Schmidt and collaborators (146 ± 7 mb) [69] and the one determined in the present experiment (149 ± 8 mb) [54] for the same reaction and energy, and also from the systematic at different energies [54]. Therefore, for the comparison of the isotopic distributions, we have normalized the values measured by Fernández-Domínguez and collaborators to the value of the total fission cross section we have measured.

This normalization was also applied in Fig. 10(b), where we compare the mass distribution of the fission fragments. As can be seen in both figures, our new measurements are in excellent agreement with the ones reported by Fernández-Domínguez (open circles) after normalization. Therefore, we can conclude that the problem with the previous measurement was only in the value of the total fission cross section. The reason for this discrepancy is not fully clear although the good agreement in the mass and charge distributions between the normalized FRS data and the present ones help us to exclude a problem with the correction applied to the FRS data because of the limited angular acceptance of the spectrometer. The discrepancy should then be caused by a wrong absolute normalization of the yields measured at the FRS.

TABLE I. Mean values and integral widths of the atomic-number distributions of the final fission fragments produced in the reactions ^{208}Pb + p, ^{nat}Pb + p, and ^{208}Pb + d at different energies.

Reaction	⟨Z⟩	σ_Z
^{208}Pb (500A MeV) + p	40.05 ± 0.20	6.27 ± 0.30
^{208}Pb (500A MeV) + p [35]	40.0 ± 0.1	6.3 ± 0.2
^{208}Pb (500A MeV) + p [57]	40.0 ± 0.5	6.6 ± 0.7
^{208}Pb (500A MeV) + d [57]	39.1 ± 0.5	7.0 ± 0.5
^{nat}Pb + p (600 MeV) [70]	40.0 ± 0.1	6.34 ± 0.1
^{208}Pb (1A GeV) + p [33]	39.6 ± 0.5	6.6 ± 0.3
^{208}Pb (1A GeV) + d [71]	39.0 ± 0.7	7.3 ± 0.5

The measurement of ^{208}Pb + p at 1A GeV performed by Enqvist and collaborators (open squares) [33] is also displayed in Figs. 10(a) and 10(b). All the measurements seem to be in good agreement although the measurement at 1A GeV shows an increase in the production of light fission fragments. This fact can be explained by the production of lighter fissioning nuclei and the larger excitation energies.

To investigate the energy dependence of the atomic- and mass-number distributions of the fission fragments, we compare our results with others obtained at different energies for similar systems. This is done in Tables I and II, where the mean values and integral widths of the atomic- and mass-number distributions are listed, respectively. The normalized values reported by Fernández-Domínguez and collaborators [35] are in excellent agreement with our results. The measurement of ^{208}Pb + p reported by Ayyad and collaborators [57] is also in agreement with our value taking its uncertainty bar into account. Our results are also in excellent agreement with the values reported by Hagebø and Lund [70], measuring the fragments produced in the fission of natural lead with protons at 600 MeV.

The reactions ^{208}Pb + d at 500A MeV [57] and 1A GeV [71], and ^{208}Pb + p at 1A GeV [33] have also been considered to complete the investigation of the energy dependence. As can be observed in the tables, the mean values of the mass- and atomic-number distributions decrease when increasing the bombarding energy. This is expected because the reactions are

TABLE II. As Table I, but for the mass-number distributions.

Reaction	⟨A⟩	σ_A
^{208}Pb (500A MeV) + p	93.1 ± 0.5	15 ± 0.6
^{208}Pb (500A MeV) + p [35]	93.0 ± 0.4	15.1 ± 0.6
^{nat}Pb + p (600 MeV) [70]	93.2 ± 0.4	14.9 ± 0.1
^{208}Pb (1A GeV) + p [33]	90.7 ± 0.4	16.1 ± 0.8
^{208}Pb (1A GeV) + d [71]	89.6 ± 1.1	17.4 ± 1.0

more violent and the number of removed nucleons increases, leading to lighter fissioning nuclei. Conversely, the integral widths increase because of the larger excitation energy.

This last feature can be explained in the framework of the statistical model [72]. According to this model the width of the atomic- and mass-number distributions of the fission fragments can be parametrized as a function of the temperature at the saddle point ($T_{\rm sad}$) as

$$\sigma_A^2 = \frac{A_{\rm fiss}^2 T_{\rm sad}}{16 d^2V/d\nu^2} \quad \text{and} \quad \sigma_Z^2 = \frac{Z_{\rm fiss}^2 T_{\rm sad}}{16 d^2V/d\nu^2}, \qquad (3)$$

where $d^2V/d\nu^2$ is the second derivative of the potential with respect to the mass-asymmetry degree of freedom at the saddle point $\nu = (4/A_{\rm fiss})/(M - A_{\rm fiss}/2)$. $A_{\rm fiss}$ and $Z_{\rm fiss}$ correspond to the mass and atomic numbers of the fissioning nucleus, respectively, and M represents the mass number of the corresponding fragment. According to these equations, the integral width increases with the excitation energy or temperature of the fissioning system at the saddle point, which is consistent with the evolution shown in the measurements. Therefore, we can conclude that the integral widths of the atomic- and mass-number distributions are dominated by the excitation energy of the fissioning system at saddle because the average atomic and mass numbers of the produced fissioning systems decrease with increasing the violence of the reaction as discussed above.

B. Mass and charge correlations between the two fission fragments

In this section, we will take advantage of the complete characterization of the two fission fragments achieved in this work to obtain additional information about the dynamical evolution of the fission process from correlations between the fragments and the fissioning systems.

The first observable we propose to characterize the properties of the fission fragments is the neutron excess of the final fragments, defined as the average neutron number $\langle N \rangle$ of a given isotopic distribution divided by its corresponding atomic number Z.

The measured neutron excess of the final fission fragments (solid circles) is displayed as a function of the atomic number in Fig. 11(a), and also compared to previous measurements of the reaction ^{208}Pb + p at 500A MeV (open circles) [35] and at 1A GeV (open squares) [33] performed at the FRS. As can be seen in the figure, our new measurement is in excellent agreement with the previous one at 500A MeV. The comparison with the measurement at 1A GeV (open squares) [33] clearly indicates that the neutron excess of the final fission fragments decreases with the reaction energy. This fact can be understood in terms of excitation energy enhancing the evaporation of neutrons and reducing the neutron excess.

The neutron excess of the fission fragments produced in both reactions (500A MeV and 1A GeV) clearly depends on their atomic number. This dependence is attributed to the modification of the average neutron excess of the fragments at scission with respect to the one of the fissioning systems, referred to as charge polarization, but also to the excitation energy sharing between the two fragments at scission. The

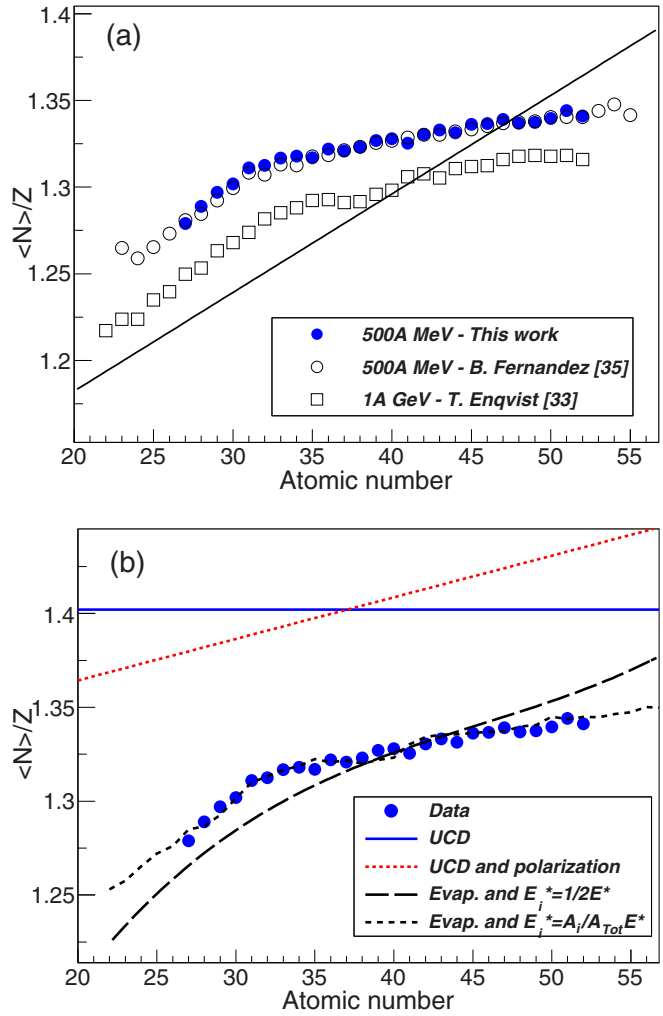

FIG. 11. (Color online) (a) Average neutron number over atomic number of the final fission fragments as a function of their atomic number. The solid circles and the open circles represent our new measurement and the data of Ref. [35] for the reaction ^{208}Pb (500A MeV) + p, respectively. The open squares correspond to the reaction ^{208}Pb (1A GeV) + p [33]. The uncertainties are shown if they exceed the size of the symbols. The solid line indicates the valley of stability (see Ref. [33]). (b) Comparison of our measurement with different model calculations.

polarization effect is explained by the exchange of protons and neutrons between the nascent fission fragments during the descent from the saddle point to scission. The neutron excess of the fragments at scission corresponds to the one giving a maximum of the saddle-to-scission released energy. In a quasistatic approximation the charge polarization can be obtained as the neutron excess of the fragments at the scission point which minimizes the forces between the nascent fragments. According to Ref. [65], such a calculation can be done from the intrinsic binding energies and mutual Coulomb repulsion for the two nascent fragments represented by two-touching spheroids.

The partition of energy between the two fission fragments and the subsequent postscission neutron evaporation also

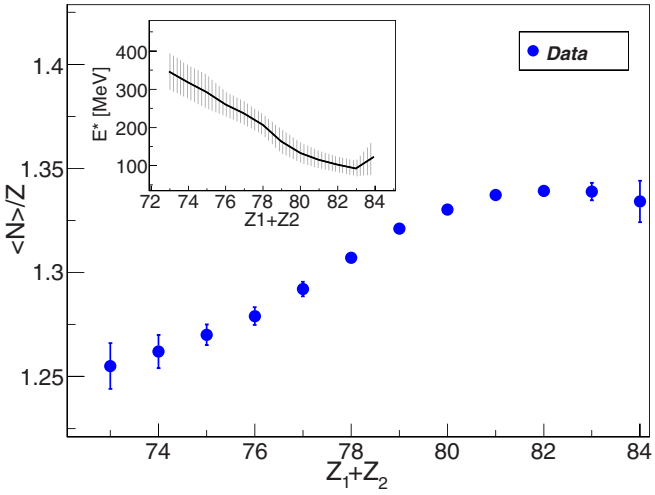

FIG. 12. (Color online) Final neutron excess of the fission fragments as a function of the atomic number of the fissioning system for the reaction ^{208}Pb (500A MeV) + p. The uncertainty bars are shown if they exceed the size of the symbols. The inset shows the excitation energy gained by the fissioning systems at the ground state as a function of their atomic number.

have a significant impact in the neutron excess of the final fission fragments, as can be seen in Fig. 11(b). For a better understanding, we compare the measured neutron excess (solid circles) with different model calculations using the code ABLA07 [62]. The solid line represents the average neutron excess of the fission fragments at the scission point calculated according to the UCD hypothesis. This estimation of the average neutron excess of the fission fragments is compared with a calculation taking into account the polarization effect (dotted line). The long- and short-dashed lines represent calculations considering the postscission neutron evaporation after a symmetric partition of excitation energy ($E_i^* = 1/2E^*$) and a partition as a function of the masses of the fission fragments at scission ($E_i^* = A_i/A_{\rm Tot}E^*$), respectively. The difference observed between the dotted and the two dashed lines can be attributed to the postscission evaporation of neutrons. As can be seen, a symmetric partition of the available excitation energy describes the neutron excess for symmetric fission fragments $Z \sim 40$ (long-dashed line), but presents a deviation for the lighter and heavier fragments. On the other hand, the energy partition as a function of the mass partition describes somewhat well the data (short-dashed line). Therefore, we can conclude that this observable is sensitive to the charge polarization effect and to the partition of excitation energy between the two fission fragments. Indeed, the best description of the data is obtained with a statistical picture, in which the fission fragments share the available excitation energy at scission according to their masses.

Our new measurement also allows us to investigate the evolution of this observable as a function of the atomic number of the fissioning system ($Z_1 + Z_2$), which presents a strong correlation with the excitation energy gained by the fissioning system at saddle [17,40,57]. As can be seen in Fig. 12 (solid circles), the neutron excess of the final fission fragments

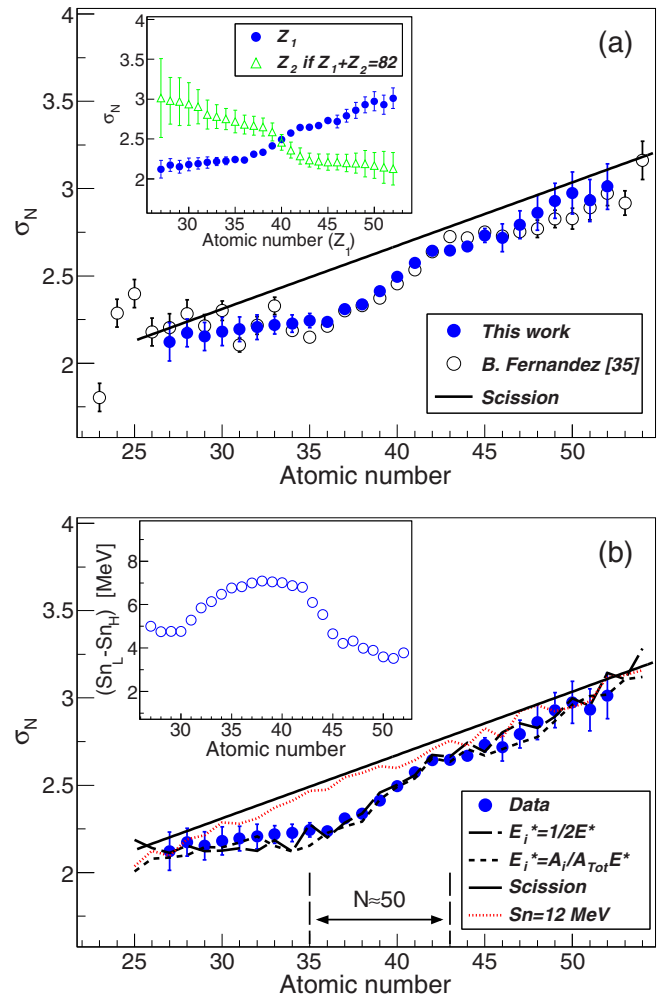

FIG. 13. (Color online) Standard deviation of the isotopic distributions as a function of the atomic number for the reaction ^{208}Pb (500A MeV) + p. The error bars are given by the uncertainty of the fit and are shown if they exceed the size of the symbols. (a) The solid and open circles represent our new measurement and the data of Ref. [35], respectively. The solid line represents standard deviation of the isotopic distributions at scission. The inset shows the standard deviation of both fission fragments (Z_1 and Z_2) measured in coincidence as a function of the atomic number of the first fission fragment (Z_1). (b) Our data are compared with different calculations (lines). (Inset) Difference between the neutron separation energy of the lightest and the heaviest fission fragment for a given element as a function of its atomic number.

decreases with the decrease of the atomic number of the fissioning system. This feature is expected because, according to the calculations shown in the inset of the figure, lighter fissioning nuclei are produced in more violent collisions [57] where the highly excited fission fragments evaporate more neutrons. Therefore, this observable is also sensitive to the excitation energy gained by the fissioning system.

Another interesting observable is the standard deviation of the isotopic distributions of the fission fragments. In Fig. 13(a) we depict the evolution of this observable as a function of the atomic number of the fission fragments (solid circles).

In the figure we also compare our data with the previous measurement performed at the FRS (open circles) [35]. One can see that both measurements are in good agreement. As expected from a statistical picture [72], the widths of the isotopic distributions of the fission fragments increase with the atomic number (solid line). In the inset of Fig. 13(a) we represent the standard deviation of the isotopic distributions for the fission fragment Z_1 (solid circles) and Z_2 (open triangles) as a function of the atomic number of the first fragment Z_1. The widths of the second fission fragment (Z_2) are conditioned by the total atomic number of the fissioning system at saddle $Z_1 + Z_2 = 82$, assuming no evaporation of protons beyond the scission point. From the data, we observe that the evolution of the widths of the isotopic distributions is symmetric as expected by atomic and mass number conservation.

In Fig. 13(b) the data are also compared with two model calculations using different prescriptions for the energy sharing between the two fission fragments. Again, the long- and short-dashed lines represent calculations using a symmetric partition of excitation energy and a partition as a function of the masses of the fission fragments at scission, respectively. Both calculations yield similar results and are in good agreement with the experimental data. We can then conclude that this observable is not sensitive to the repartition of the excitation energy between the fission fragments at the scission point.

The difference between the measured widths and the ones calculated at the scission point (solid line) could be from structural effects affecting the last steps of the postscission neutron evaporation. Indeed, the slope change observed between $Z = 35$ and $Z = 43$ could be attributed to the neutron shell $N = 50$. These isotopic chains cross the $N = 50$ shell. Isotopes close to this shell present larger binding energies, preventing neutron evaporation. The inset in Fig. 13(b) illustrates this effect displaying the difference between the maximum and minimum binding energy in the isotopic chains of the fission fragments measured in this work as a function of their atomic number. This effect reduces the widths of the isotopic distribution of the fission fragments with respect to the calculated ones at scission (solid line). To validate this interpretation, we also calculated the widths of the isotopic distribution considering a constant value of the neutron separation energy of $S_n = 12$ MeV for all the fission fragments (dotted line). One can observe that this calculation does not present large deviations with respect to the one at scission. Therefore, the slope changes observed in the widths of the isotopic distribution can only be attributed to the larger neutron separation energies for the fission fragments crossing the neutron shell $N = 50$.

In Fig. 14, we display again the evolution of the widths of the isotopic distributions as a function of the atomic number of the fission fragments, but this time for two different fissioning systems: $Z_1 + Z_2 = 82$ (solid triangles) and $Z_1 + Z_2 = 76$ (open triangles). As can be seen in the figure, the widths of the isotopic distributions of the fissioning system $Z_1 + Z_2 = 76$ are larger than the ones measured for the fissioning system $Z_1 + Z_2 = 82$. The data are also compared with ABLA07 [62] calculations. The calculations show similar evolutions under the same conditions. This tendency would be explained by the fact that the fissioning systems with smaller atomic number

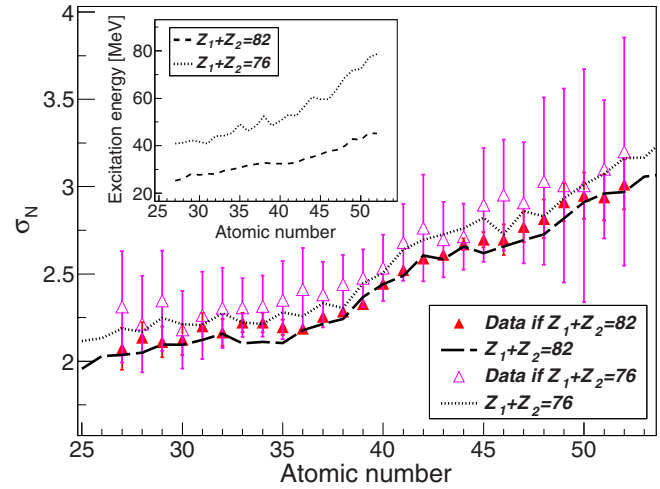

FIG. 14. (Color online) Standard deviation of the isotopic distributions as a function of the atomic number of the fission fragments for two fissioning systems: $Z_1 + Z_2 = 82$ (solid triangles) and $Z_1 + Z_2 = 76$ (open triangles). The lines represent ABLA07 [62] calculations for the same fissioning systems: $Z_1 + Z_2 = 82$ (long-dashed line) and $Z_1 + Z_2 = 76$ (dotted line). The inset shows the calculated excitation energy of the fission fragments at scission as a function of the atomic number of the final fission fragments for the fissioning systems $Z_1 + Z_2 = 82$ (long-dashed line) and $Z_1 + Z_2 = 76$ (dotted line).

gain more excitation energy than the ones with larger values of atomic number. To validate this hypothesis, in the inset of the figure we represent the calculated mean excitation energy of the fission fragments as a function of their atomic number. One can observe that the mean excitation energy for $Z_1 + Z_2 = 76$ is always larger for all atomic numbers of the fission fragments. In both cases we observe, however, similar slope changes in the evolution of the widths of the isotopic distributions as a function of the corresponding atomic number. Therefore, we can confirm that this observable is sensitive to the total excitation energy gained by the fissioning system and to structural effects in the fission fragments, but not to the share of the excitation energy between the two fragments.

C. Velocities of the fission fragments

The reconstructed path length of the nuclei traversing the experimental setup together with the ToF measurements were used to obtain the velocity of the fission fragments in the laboratory frame. These velocities can then be transformed into the reference frame defined by the velocity of the incoming projectiles in the center of the target using the corresponding Lorentz transformation. The experimental setup allows for a precise reconstruction of the laboratory angles of the fission fragments (better than 0.4 mrad), and therefore the measurement of the velocity is performed with a good accuracy (better than 5%) in the reference frame of the incoming projectiles.

Fission velocities provide information on the Coulomb repulsion experienced by the fission fragments at the scission point. Therefore, one could use these velocities to assess

the distance between the two fission fragments formed at the scission point. According to the semistatistical scission point model of Wilkins and collaborators [73], the main contribution to the total kinetic energies released in the fission process comes from the Coulomb repulsion of the two fission fragments at the scission point and, therefore, this total kinetic energy is given by

$$TKE \sim \frac{Z_1 Z_2}{D}, \tag{4}$$

where Z_1 and Z_2 refer to the atomic number of the two fission fragments and D is the distance between the two uniformly charged spheroids representing the fission fragments. This distance is parametrized as

$$D = r_0 A_1^{1/3}\left(1 + \frac{2\beta_1}{3}\right) + r_0 A_2^{1/3}\left(1 + \frac{2\beta_2}{3}\right) + d, \tag{5}$$

where A_1 and A_2 refer to the mass number of the two fission fragments, β_1 and β_2 are their quadrupole deformations at the scission point, r_0 is the fermi radius, and d is the tip distance between the two fission fragments.

Following this semistatistical approach, the fission velocity can be written as

$$V_{\rm fiss} = \left[\frac{2Z_1 Z_2}{A_1\left(1 + \frac{A_1}{A_2}\right)D}\right]^{1/2}. \tag{6}$$

Equations (4)–(6) are included in the fission model of ABLA07 [62] to calculate the fission velocities of the fission fragments.

It is well known that one of the parameters affecting the velocity gained by the fission fragments is the tip distance d. In the pioneering work of Wilkins and collaborators [73] a standard tip distance $d = 2$ fm was proposed. Recent works [39] based on measurements of the total kinetic energy, using constant values for the quadrupole deformation at the scission point ($\beta_1 = \beta_2 = 0.625$), have also found a similar value for the tip distance. In other works, the authors have found that the tip distance has an upper limit around 3 fm [74,75], where larger values are considered as invalid configurations. This upper limit is consistent with the values recently found by the authors of Ref. [76], where a dependence of the tip distance d with the Coulomb-repulsion term of the LDM was observed.

In Fig. 15 we display the average velocities of the fission fragments as a function of their atomic number (open triangles). As can be seen in the figure, the fission velocities decrease with the atomic number of the fission fragments, which is a natural consequence of the momentum conservation between the light and the heavy fission fragment. In the same figure, our measurement is compared with different calculations based on the proposed value for the tip distance $d = 2$ fm (dashed line), the found upper limit $d = 3$ fm (dotted line), and $d = 1$ fm (solid line). One can observe that these calculations provide similar results with a difference smaller than 7%. Therefore, one can conclude that the mean fission velocities of the fission fragments as a function of their atomic numbers present a limited sensitivity to the tip distance between the two fission fragments at scission. This result confirms the need of additional observables to further investigate this issue.

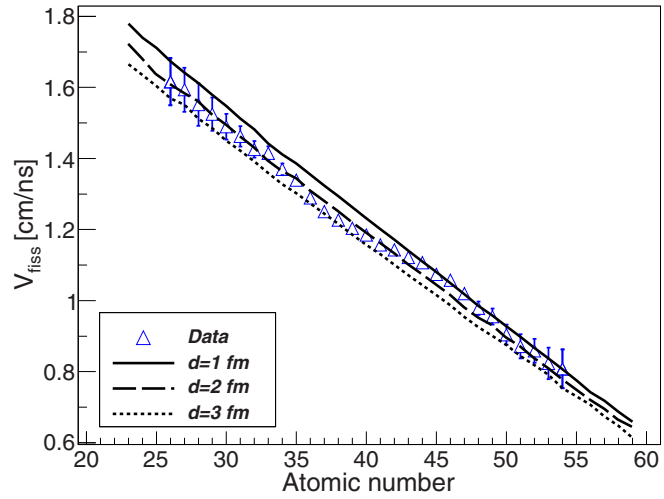

FIG. 15. (Color online) Mean fission velocity of the fission fragments as a function of the atomic number of the fission fragments for the reaction ^{208}Pb (500A MeV) + p. The lines represent different calculations.

Equation (6) indicates a clear dependence of the fission velocity on the total charge of the fissioning system at scission. Therefore, in Fig. 16(a) we display the average fission velocities of the fission fragments as a function of the atomic number of the fissioning nucleus (solid circles). Surprisingly, the velocities do not depend very much on the size of the fissioning system. To understand this result, we compare our data with different model calculations, in particular with one using a tip distance between the fission fragments at scission of $d = 2$ fm (dotted line). As can be seen in the figure, this calculation cannot describe the evolution of the data, and shows a clear deviation for the lighter fissioning nuclei ($Z_1 + Z_2 < 78$).

To understand this discrepancy, we also compare our measurement with different calculations changing the mass and atomic numbers of the fission fragments. The calculations performed with $A - 1$ (dot-dashed line) and $A + 1$ (dot-long-dashed line) do not show any sizable difference with respect to standard ones, while the calculations assuming $Z - 1$ (double-dot-dashed line) and $Z + 1$ (long-dashed line) present offsets that can be explained with the decrease and increase of the Coulomb repulsion, respectively, but none of them provides a satisfactory description of the data. From these calculations we conclude that the discrepancy observed between the standard calculations and our data cannot be explained with simple variations of the atomic or mass number of the fission fragments at scission.

Following Ref. [76], the tip distance between the two fission fragments increases with the repulsion term $Z^2/A^{1/3}$ and then with the atomic number of the fissioning system. This fact indicates that the tip distance is expected to increase with the atomic number of the fissioning nuclei. Based on this idea, we performed calculations using a tip distance of 1 fm to try to describe the mean fission velocities of the lighter fissioning system, taking into account that calculations with $d = 2$ fm can reproduce the velocities of the heavier fissioning nuclei ($Z_1 + Z_2 \sim 82$). As can be seen in the figure, this calculation

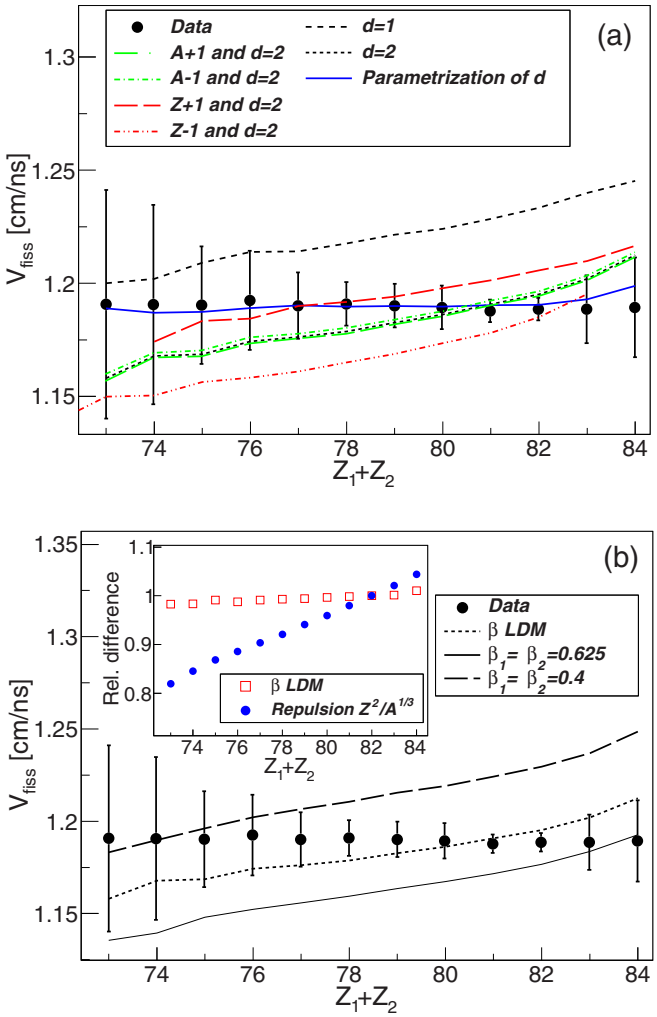

FIG. 16. (Color online) Mean fission velocity of the fission fragments in the reference frame of the fissioning system for the reaction ^{208}Pb (500A MeV) + p as a function of the atomic number of the fissioning system. (a) The lines represent different calculations changing some variables such as the atomic and mass number of the fission fragments, as well as the tip distance d. (b) The lines indicate calculations for different values of the deformation at the scission point. The inset shows how the quadrupole deformation of the fission fragments and Coulomb repulsion evolve with the atomic number of the fissioning system.

overestimates our measurement for the heaviest fissioning nuclei, but seems to be in agreement with the mean fission velocities obtained for the lightest ones. These calculations seem to point out a dependence of the tip distance with the size of the fissioning system and, thus, we implemented such a dependence in our calculations. Equation (7) represents the used parametrization, where d is the tip distance and $Z^{\rm sci}_{\rm fiss}$ the atomic number of the fissioning system at the scission point:

$$d = -8.125 + 0.125 Z^{\rm sci}_{\rm fiss}. \quad (7)$$

The result of the calculation using this parametrization is also represented in Fig. 16(a) (solid line), describing somewhat well the data.

However, the distance between the two fission fragments also depends on their quadrupole deformations [see Eq. (5)]. This issue is investigated in Fig. 16(b), where the data are compared with different calculations. The solid line represents a calculation using a constant quadrupole deformation of $\beta = 0.625$ for both fission fragments, while the dashed line represents the same calculation but for a constant quadrupole deformation of $\beta = 0.4$. This reduction of the deformation could also explain the increase of the average fission velocities. However, the fission fragments produced for the different fissioning systems are somewhat similar in size and therefore in deformation. This result is displayed in the inset of the figure, where the evolution of the average quadrupole deformation as predicted by the LDM for the fission fragments at scission [73] is represented relative to the value obtained for the fissioning systems $Z_1 + Z_2 = 82$ as a function of the atomic number of the fissioning system (open squares). As can be seen, the difference in percent between the mean deformations as a function of $Z_1 + Z_2$ is below 2%. In the same inset, we also display the evolution of the average Coulomb-repulsion term $Z^2/A^{1/3}$ of the fissioning systems (solid circles), which changes a factor around 20% between $Z_1 + Z_2 = 82$ and $Z_1 + Z_2 = 73$. This fact, together with the negligible change on quadrupole deformation, favors the idea of a variation of the tip distance with the atomic number of the fissioning system. We conclude that a change of the distance between the two fission fragments is needed to explain the evolution of the average fission velocities as a function of the size of the fissioning system.

IV. SUMMARY AND CONCLUSIONS

In the present work, we have investigated proton-induced fission of ^{208}Pb in inverse kinematics at 500A MeV using a highly efficient detection setup that permitted one for the first time to measure in coincidence the mass and atomic number of the two fission fragments with good resolution.

The atomic-number distributions of the fission fragments are obtained from energy loss measurements in a double multisampling ionization chamber (twin MUSIC) with a resolution below 0.43 charge units (FWHM), while the mass numbers are obtained from the mass-over-charge ratio (A/Z) determined from magnetic rigidity and time-of-flight measurements with a resolution of 40 ps (FWHM). This measurement provides the complete isotopic distribution of fission fragments from cobalt to tellurium with an average mass-number resolution of $\Delta A \sim 0.6$ mass units (FWHM).

These new data are used to validate previous controversial measurements of the same isotopic distributions and to study their properties, such as the mean neutron excess and the widths of the distributions, but also the velocities of the final fission fragments.

Moreover, our measurement allows us to investigate the mass and charge correlations between the two fission fragments. We investigated the evolution of the average neutron excess and the width of the isotopic distributions of the final fission fragments as a function of the atomic number of the fissioning nuclei. Different model calculations of the neutron excess indicate that this observable is sensitive to the

polarization effect, the postscission neutron evaporation and the partition of the excitation energy between the two fission fragments at scission. Our calculations helped us to conclude that a partition of excitation energy as a function of the masses of the fission fragments provides a better description of the data. We also observe that the neutron excess of the fission fragments decreases with decreasing the atomic number of the fissioning system. This fact can be explained by an increase of the excitation energy for the lighter fissioning systems at the saddle point [17,40,57].

On the other hand, we showed that the widths of the isotopic distributions are sensitive to the total excitation energy gained by the fissioning system and to structural effects in the deexcitation of fission fragments crossing the neutron shell $N = 50$. The slope changes observed in the widths of the isotopic distribution can only be explained by the larger neutron separation energies for the fission fragments crossing the neutron shell $N = 50$.

In addition, our data are used to investigate the velocities of the fission fragments at the scission point as a function of the atomic number of the fissioning system. The comparison with different model calculations for the fissioning nuclei investigated in this work allows us to conclude that the velocities of the fragments as a function of the size of the fissioning nuclei are more sensitive to the tip distance between the fission fragments than to their quadrupole deformations. Finally, we have parametrized the value of the tip distance as a function of the size of the fissioning nuclei.

ACKNOWLEDGMENTS

The authors are grateful to the GSI accelerator staff for providing an intense and stable beam of ^{208}Pb. We also gratefully acknowledge J.-M. Gheller and S. Leray for providing the liquid hydrogen target and G. Ickert, D. Körper, N. Kurz, and A. Prochazka for their technical support during the experiment. This work was partially supported by the European Commission under Projects No. ANDES-FP7-249671 and No. CHANDA-FP7-605203, the Spanish Ministry of Research and Innovation under Projects No. FPA2010-22174-C02 and No. Consolider-CPAN-CSD2007-00042, and the Regional Government of Galicia under the program "Grupos de Referencia Competitiva 2013-011." One of us, C.R.T., also acknowledges the support of the Spanish Ministry of Education under a grant of postdoctoral mobility (2011) administered by FECYT.

APPENDIX: ISOTOPIC CROSS SECTIONS

The isotopic cross sections of the fission fragments measured in the reaction ^{208}Pb + p at 500A MeV are listed in Table III with their associated uncertainties.

TABLE III. Isotopic cross sections of the fission fragments measured in the reaction ^{208}Pb (500A MeV) + p with their associated statistical and systematical uncertainties indicated in parentheses, respectively.

Z	A	σ (mb)	Z	A	σ (mb)	Z	A	σ (mb)
27	58	0.103(0.025)(0.004)	27	59	0.261(0.024)(0.009)	27	60	0.356(0.025)(0.012)
27	61	0.480(0.032)(0.017)	27	62	0.443(0.033)(0.016)	27	63	0.367(0.028)(0.013)
27	64	0.233(0.021)(0.008)	27	65	0.145(0.016)(0.005)	28	60	0.082(0.020)(0.003)
28	61	0.263(0.035)(0.009)	28	62	0.464(0.035)(0.015)	28	63	0.620(0.040)(0.020)
28	64	0.577(0.032)(0.019)	28	65	0.501(0.028)(0.016)	28	66	0.394(0.023)(0.013)
28	67	0.253(0.021)(0.008)	28	68	0.154(0.023)(0.005)	29	63	0.237(0.020)(0.007)
29	64	0.391(0.024)(0.012)	29	65	0.658(0.033)(0.020)	29	66	0.735(0.036)(0.023)
29	67	0.756(0.037)(0.023)	29	68	0.641(0.033)(0.019)	29	69	0.424(0.029)(0.013)
29	70	0.207(0.018)(0.007)	30	64	0.065(0.010)(0.002)	30	65	0.152(0.013)(0.004)
30	66	0.381(0.021)(0.011)	30	67	0.703(0.032)(0.020)	30	68	0.919(0.037)(0.027)
30	69	0.909(0.039)(0.026)	30	70	0.696(0.031)(0.020)	30	71	0.548(0.031)(0.016)
30	72	0.342(0.021)(0.010)	30	73	0.222(0.022)(0.006)	30	74	0.116(0.016)(0.003)
31	66	0.073(0.011)(0.002)	31	67	0.158(0.013)(0.004)	31	68	0.334(0.020)(0.009)
31	69	0.587(0.023)(0.016)	31	70	1.05(0.04)(0.03)	31	71	1.16(0.04)(0.03)
31	72	1.03(0.04)(0.03)	31	73	0.751(0.028)(0.020)	31	74	0.553(0.024)(0.015)
31	75	0.321(0.019)(0.009)	31	76	0.139(0.012)(0.004)	31	77	0.054(0.009)(0.002)
32	69	0.130(0.012)(0.003)	32	70	0.370(0.021)(0.010)	32	71	0.737(0.031)(0.019)
32	72	1.27(0.04)(0.03)	32	73	1.53(0.05)(0.04)	32	74	1.30(0.04)(0.03)
32	75	1.03(0.03)(0.03)	32	76	0.815(0.033)(0.020)	32	77	0.511(0.024)(0.013)
32	78	0.273(0.020)(0.007)	32	79	0.109(0.012)(0.003)	33	72	0.160(0.011)(0.004)
33	73	0.748(0.031)(0.018)	33	74	1.29(0.04)(0.03)	33	75	1.69(0.05)(0.04)
33	76	1.70(0.04)(0.04)	33	77	1.73(0.04)(0.04)	33	78	1.34(0.04)(0.03)
33	79	0.962(0.034)(0.023)	33	80	0.545(0.029)(0.013)	33	81	0.257(0.017)(0.006)
34	74	0.201(0.013)(0.005)	34	75	0.623(0.031)(0.014)	34	76	1.38(0.05)(0.03)
34	77	1.91(0.05)(0.04)	34	78	2.20(0.05)(0.05)	34	79	2.00(0.04)(0.05)
34	80	1.69(0.04)(0.04)	34	81	1.11(0.03)(0.03)	34	82	0.731(0.029)(0.017)
34	83	0.387(0.026)(0.010)	35	76	0.139(0.011)(0.004)	35	77	0.482(0.022)(0.011)

TABLE III. *(Continued.)*

Z	A	σ (mb)	Z	A	σ (mb)	Z	A	σ (mb)
35	78	0.964(0.039)(0.021)	35	79	1.56(0.05)(0.04)	35	80	2.01(0.05)(0.04)
35	81	2.43(0.05)(0.05)	35	82	2.36(0.05)(0.05)	35	83	1.90(0.05)(0.04)
35	84	1.31(0.04)(0.03)	35	85	0.535(0.024)(0.012)	35	86	0.236(0.020)(0.005)
36	78	0.109(0.008)(0.003)	36	79	0.417(0.023)(0.009)	36	80	1.13(0.04)(0.02)
36	81	2.09(0.06)(0.04)	36	82	2.40(0.05)(0.05)	36	83	2.49(0.05)(0.05)
36	84	2.48(0.05)(0.05)	36	85	2.18(0.05)(0.05)	36	86	1.40(0.04)(0.03)
36	87	0.785(0.032)(0.018)	36	88	0.388(0.024)(0.008)	36	89	0.109(0.012)(0.002)
37	80	0.052(0.004)(0.001)	37	81	0.315(0.018)(0.007)	37	82	0.946(0.035)(0.020)
37	83	1.47(0.04)(0.03)	37	84	2.38(0.052)(0.049)	37	85	2.64(0.049)(0.055)
37	86	2.76(0.052)(0.057)	37	87	2.61(0.052)(0.054)	37	88	1.78(0.049)(0.037)
37	89	1.04(0.034)(0.022)	37	90	0.525(0.024)(0.011)	37	91	0.294(0.018)(0.006)
37	92	0.095(0.010)(0.002)	38	82	0.073(0.009)(0.001)	38	83	0.209(0.012)(0.005)
38	84	0.627(0.021)(0.013)	38	85	1.32(0.03)(0.03)	38	86	2.13(0.04)(0.04)
38	87	2.63(0.05)(0.05)	38	88	2.89(0.05)(0.06)	38	89	2.76(0.06)(0.06)
38	90	2.29(0.05)(0.05)	38	91	1.45(0.04)(0.03)	38	92	1.14(0.04)(0.02)
38	93	0.438(0.020)(0.009)	38	94	0.105(0.009)(0.002)	39	84	0.033(0.007)(0.001)
39	85	0.109(0.007)(0.002)	39	86	0.449(0.018)(0.009)	39	87	1.20(0.03)(0.02)
39	88	2.08(0.04)(0.04)	39	89	2.60(0.04)(0.05)	39	90	2.83(0.05)(0.06)
39	91	2.91(0.06)(0.06)	39	92	2.53(0.05)(0.05)	39	93	1.87(0.05)(0.04)
39	94	0.937(0.026)(0.019)	39	95	0.877(0.030)(0.018)	39	96	0.391(0.020)(0.007)
39	97	0.175(0.012)(0.004)	40	86	0.036(0.008)(0.001)	40	87	0.107(0.010)(0.002)
40	88	0.319(0.013)(0.007)	40	89	0.860(0.024)(0.017)	40	90	1.59(0.03)(0.03)
40	91	2.48(0.05)(0.05)	40	92	2.71(0.05)(0.05)	40	93	2.81(0.05)(0.06)
40	94	2.65(0.05)(0.05)	40	95	2.43(0.05)(0.05)	40	96	1.26(0.03)(0.03)
40	97	0.927(0.030)(0.018)	40	98	0.535(0.023)(0.011)	40	99	0.246(0.017)(0.005)
40	100	0.107(0.012)(0.002)	40	101	0.037(0.006)(0.001)	41	88	0.023(0.009)(0.001)
41	89	0.112(0.012)(0.002)	41	90	0.374(0.021)(0.008)	41	91	0.766(0.024)(0.015)
41	92	1.28(0.03)(0.03)	41	93	1.88(0.04)(0.04)	41	94	2.96(0.06)(0.06)
41	95	2.63(0.05)(0.05)	41	96	2.67(0.05)(0.05)	41	97	2.52(0.05)(0.05)
41	98	1.66(0.04)(0.03)	41	99	1.13(0.03)(0.02)	41	100	0.632(0.024)(0.013)
41	101	0.306(0.015)(0.006)	41	102	0.088(0.007)(0.002)	41	103	0.012(0.002)(0.001)
42	89	0.011(0.001)(0.001)	42	90	0.028(0.016)(0.001)	42	91	0.110(0.016)(0.002)
42	92	0.294(0.016)(0.006)	42	93	0.661(0.027)(0.013)	42	94	1.02(0.03)(0.02)
42	95	1.34(0.03)(0.03)	42	96	2.12(0.05)(0.04)	42	97	2.26(0.04)(0.05)
42	98	2.52(0.05)(0.05)	42	99	2.53(0.05)(0.05)	42	100	2.23(0.05)(0.04)
42	101	1.62(0.04)(0.03)	42	102	0.805(0.026)(0.016)	42	103	0.478(0.021)(0.010)
42	104	0.129(0.009)(0.003)	42	105	0.045(0.006)(0.001)	43	93	0.066(0.007)(0.001)
43	94	0.174(0.014)(0.004)	43	95	0.317(0.018)(0.007)	43	96	0.762(0.029)(0.016)
43	97	1.19(0.03)(0.02)	43	98	1.87(0.04)(0.04)	43	99	2.10(0.04)(0.04)
43	100	2.34(0.05)(0.05)	43	101	2.24(0.05)(0.05)	43	102	2.13(0.05)(0.04)
43	103	1.79(0.04)(0.04)	43	104	1.14(0.03)(0.02)	43	105	0.444(0.018)(0.009)
43	106	0.252(0.016)(0.005)	43	107	0.120(0.011)(0.003)	44	95	0.053(0.008)(0.001)
44	96	0.155(0.015)(0.003)	44	97	0.238(0.016)(0.005)	44	98	0.580(0.024)(0.012)
44	99	0.962(0.028)(0.020)	44	100	1.63(0.04)(0.04)	44	101	1.88(0.04)(0.04)
44	102	2.05(0.04)(0.04)	44	103	2.22(0.05)(0.05)	44	104	2.00(0.04)(0.04)
44	105	1.61(0.04)(0.03)	44	106	1.10(0.03)(0.02)	44	107	0.735(0.029)(0.016)
44	108	0.318(0.017)(0.007)	44	109	0.105(0.009)(0.002)	44	110	0.041(0.005)(0.001)
45	97	0.031(0.011)(0.001)	45	98	0.092(0.016)(0.002)	45	99	0.220(0.020)(0.005)
45	100	0.267(0.014)(0.006)	45	101	0.723(0.027)(0.016)	45	102	1.10(0.03)(0.02)
45	103	1.52(0.04)(0.03)	45	104	1.64(0.04)(0.04)	45	105	1.97(0.04)(0.04)
45	106	1.93(0.05)(0.04)	45	107	1.69(0.04)(0.04)	45	108	1.34(0.04)(0.03)
45	109	0.904(0.036)(0.020)	45	110	0.390(0.021)(0.009)	45	111	0.175(0.012)(0.0039)
45	112	0.051(0.006)(0.001)	46	100	0.053(0.014)(0.001)	46	101	0.105(0.015)(0.002)
46	102	0.211(0.014)(0.005)	46	103	0.421(0.018)(0.010)	46	104	0.865(0.032)(0.020)
46	105	1.28(0.04)(0.03)	46	106	1.61(0.04)(0.04)	46	107	1.77(0.04)(0.04)
46	108	1.60(0.04)(0.04)	46	109	1.40(0.04)(0.03)	46	110	1.20(0.04)(0.03)

TABLE III. *(Continued.)*

Z	A	σ (mb)	Z	A	σ (mb)	Z	A	σ (mb)
46	111	0.926(0.038)(0.022)	46	112	0.526(0.023)(0.012)	46	113	0.211(0.012)(0.005)
46	114	0.084(0.008)(0.002)	46	115	0.042(0.007)(0.001)	47	104	0.151(0.011)(0.004)
47	105	0.311(0.016)(0.008)	47	106	0.613(0.025)(0.015)	47	107	0.984(0.031)(0.024)
47	108	1.26(0.04)(0.03)	47	109	1.38(0.04)(0.03)	47	110	1.39(0.04)(0.03)
47	111	1.33(0.04)(0.03)	47	112	1.23(0.04)(0.03)	47	113	0.934(0.033)(0.023)
47	114	0.522(0.023)(0.013)	47	115	0.231(0.014)(0.006)	47	116	0.131(0.011)(0.003)
47	117	0.070(0.010)(0.002)	48	106	0.100(0.024)(0.003)	48	107	0.212(0.021)(0.005)
48	108	0.479(0.027)(0.012)	48	109	0.785(0.036)(0.020)	48	110	0.984(0.040)(0.025)
48	111	1.10(0.04)(0.03)	48	112	1.11(0.04)(0.03)	48	113	1.10(0.03)(0.03)
48	114	1.02(0.04)(0.03)	48	115	0.845(0.032)(0.022)	48	116	0.669(0.028)(0.017)
48	117	0.299(0.018)(0.008)	48	118	0.105(0.009)(0.003)	49	109	0.193(0.026)(0.005)
49	110	0.324(0.026)(0.009)	49	111	0.505(0.031)(0.014)	49	112	0.680(0.035)(0.018)
49	113	0.822(0.033)(0.022)	49	114	0.951(0.040)(0.026)	49	115	0.909(0.035)(0.025)
49	116	0.891(0.038)(0.024)	49	117	0.755(0.033)(0.021)	49	118	0.524(0.026)(0.014)
49	119	0.253(0.014)(0.007)	49	120	0.133(0.011)(0.004)	49	121	0.084(0.010)(0.002)
50	112	0.147(0.017)(0.004)	50	113	0.291(0.023)(0.008)	50	114	0.423(0.025)(0.012)
50	115	0.632(0.031)(0.018)	50	116	0.668(0.030)(0.019)	50	117	0.759(0.035)(0.022)
50	118	0.729(0.033)(0.021)	50	119	0.662(0.030)(0.019)	50	120	0.529(0.028)(0.015)
50	121	0.341(0.024)(0.009)	51	114	0.107(0.012)(0.003)	51	115	0.207(0.020)(0.006)
51	116	0.284(0.019)(0.090)	51	117	0.392(0.026)(0.012)	51	118	0.497(0.030)(0.015)
51	119	0.553(0.029)(0.017)	51	120	0.568(0.030)(0.018)	51	121	0.562(0.032)(0.017)
51	122	0.457(0.027)(0.014)	51	123	0.340(0.021)(0.010)	51	124	0.185(0.016)(0.006)
51	125	0.078(0.009)(0.002)	52	116	0.084(0.015)(0.003)	52	117	0.144(0.020)(0.005)
52	118	0.192(0.021)(0.007)	52	119	0.266(0.022)(0.008)	52	120	0.329(0.023)(0.011)
52	121	0.381(0.024)(0.012)	52	122	0.464(0.033)(0.015)	52	123	0.401(0.026)(0.013)
52	124	0.327(0.020)(0.011)	52	125	0.226(0.018)(0.007)	52	126	0.164(0.014)(0.005)
52	127	0.086(0.010)(0.003)	52	128	0.034(0.005)(0.001)			

[1] China Spallation Neutron Source (CSNS) [http://csns.ihep.ac.cn/english/index.htm].
[2] European Spallation Source [http://europeanspallationsource.se/].
[3] H. Nifenecker, S. David, J. M. Loiseaux, and O. Meplan, Nucl. Instrum. Methods Phys. Res., Sect. A **463**, 428 (2001).
[4] I. Tanihata, Nucl. Phys. A **685**, 80c (2001).
[5] A. C. Mueller, Prog. Part. Nucl. Phys. **46**, 359 (2001).
[6] M. Lewitowicz, J. Phys.: Conf. Ser. **312**, 052014 (2011).
[7] J. R. Arnold *et al.*, J. Geophys. Res. **66**, 3519 (1961).
[8] A. Boudard, J. Cugnon, S. Leray, and C. Volant, Phys. Rev. C **66**, 044615 (2002).
[9] K. H. Bhatt, P. Grangé, and B. Hiller, Phys. Rev. C **33**, 954 (1986).
[10] D. Hilsher and H. Rossner, Ann. Phys. (Paris) **17**, 471 (1992).
[11] D.J. Hofman, B.B. Back, I. Dioszegi, C.P. Montoya, S. Schadmand, R. Varma, and P. Paul, Phys. Rev. Lett. **72**, 470 (1994).
[12] J. P. Lestone, Phys. Rev. Lett. **70**, 2245 (1993).
[13] N. Bohr and J. A. Wheeler, Phys. Rev. **56**, 426 (1939).
[14] J. P. Lestone and S. G. McCalla, Phys. Rev. C **79**, 044611 (2009).
[15] P. Grangé, Li Jun-Qing, and H. A. Weidenmller, Phys. Rev. C **27**, 2063 (1983).
[16] B. Jurado, C. Schmitt, K. H. Schmidt, J. Benlliure, and A. R. Junghans, Nucl. Phys. A **747**, 14 (2005).
[17] B. Jurado, C. Schmitt, K. H. Schmidt, J. Benlliure, T. Enqvist, A. R. Junghans, A. Kelić, and F. Rejmund, Phys. Rev. Lett. **93**, 072501 (2004).
[18] Y. Ayyad *et al.*, Phys. Rev. C **89**, 054610 (2014).
[19] E. Moll *et al.*, Nucl. Instrum. Methods **139**, 213 (1976).
[20] G. Siegert, H. Wollnik, J. Greif, R. Decker, G. Fiedler, and B. Pfeiffer, Phys. Rev. C **14**, 1864 (1976).
[21] W. Lang, H. G. Clerc, H. Wohlfarth, H. Schrader, and K. H. Schmidt, Nucl. Phys. A **345**, 34 (1980).
[22] U. Quade *et al.*, Nucl. Phys. A **487**, 1 (1988).
[23] C. Schmitt *et al.*, Nucl. Phys. A **430**, 21 (1984).
[24] D. Rochman *et al.*, Nucl. Phys. A **710**, 3 (2002).
[25] M. Djebara *et al.*, Nucl. Phys. A **496**, 346 (1989).
[26] A. Turkevich and J. B. Niday, Phys. Rev. **84**, 52 (1951).
[27] I. Nishinaka *et al.*, Phys. Rev. C **56**, 891 (1997).
[28] A. Bail *et al.*, Phys. Rev. C **84**, 034605 (2011).
[29] J. Elseviers *et al.*, Phys. Rev. C **88**, 044321 (2013).
[30] H. Geissel *et al.*, Nucl. Instrum. Methods Phys. Res., Sect. B **70**, 286 (1992).
[31] J. Benlliure, E. Casarejos, J. Pereira, and K. H. Schmidt, Phys. Rev. C **74**, 014609 (2006).
[32] J. Benlliure, A. Grewe, M. de Jong, K. H. Schmidt, and S. Zhdanov, Nucl. Phys. A **628**, 458 (1998).
[33] T. Enqvist *et al.*, Nucl. Phys. A **686**, 481 (2001).
[34] M. Bernas *et al.*, Nucl. Phys. A **725**, 213 (2003).

[35] B. Fernández-Domínguez *et al.*, Nucl. Phys. A **747**, 227 (2005).
[36] J. Pereira, P. Armbruster, J. Benlliure, and K. H. Schmidt, Phys. Rev. C **75**, 044604 (2007).
[37] K. H. Schmidt *et al.*, Nucl. Phys. A **665**, 221 (2000).
[38] K. H. Schmidt, J. Benlliure, and A. R. Junghans, Nucl Phys. A **693**, 169 (2001).
[39] C. Böckstiegel, S. Steinhäuser, J. Benlliure, H. G. Clerc, A. Grewe, A. Heinz, M. de Jong, A. R. Junghans, J. Müller, and K. H. Schmidt, Phys. Lett. B **398**, 259 (1997).
[40] C. Schmitt, K. H. Schmidt, A. Kelić, A. Heinz, B. Jurado, and P. N. Nadtochy, Phys. Rev. C **81**, 064602 (2010).
[41] F. Farget *et al.*, J. Phys.: Conf. Ser. **420**, 012119 (2013).
[42] M. Caamano, O. Delaune, F. Farget, X. Derkx, K.-H. Schmidt, L. Audouin, C.-O. Bacri, G. Barreau, J. Benlliure, E. Casarejos, A. Chbihi, B. Fernandez-Dominguez, L. Gaudefroy, C. Golabek, B. Jurado, A. Lemasson, A. Navin, M. Rejmund, T. Roger, A. Shrivastava, and C. Schmitt, Phys. Rev. C **88**, 024605 (2013).
[43] C. Rodríguez-Tajes *et al.*, Phys. Rev. C **89**, 024614 (2014).
[44] H. Savajols (VAMOS Collaboration), Nucl. Instrum. Methods Phys. Res., Sect. B **204**, 146 (2003).
[45] T. Gorbinet *et al.*, Phys. Procedia **64**, 101 (2015).
[46] G. Boutoux *et al.*, Phys. Procedia **47**, 166 (2013).
[47] J. L. Rodríguez-Sánchez *et al.*, EPJ Web Conf. **62**, 07009 (2013).
[48] E. Pellereau *et al.*, EPJ Web Conf. **62**, 06005 (2013).
[49] A. Ebran *et al.*, Nucl. Instrum. Methods Phys. Res., Sect. A **728**, 40 (2013).
[50] M. Pfüzner *et al.*, Nucl. Instrum. Methods Phys. Res., Sect. B **86**, 213 (1994).
[51] R. Janik *et al.*, Nucl. Instrum. Methods Phys. Res., Sect. A **640**, 54 (2011).
[52] B. Voss, *Proceedings of the Nuclear Science Symposium and Medical Imaging Conference* (NSS/MIC-IEEE, Valencia, Spain, 2011).
[53] C. Finck *et al.*, J. Phys.: Conf. Ser. **50**, 397 (2006).
[54] J. L. Rodríguez-Sánchez *et al.*, Phys. Rev. C **90**, 064606 (2014).
[55] A. Kelić *et al.*, Phys. Rev. C **70**, 064608 (2004).
[56] L. Audouin *et al.*, Nucl. Phys. A **768**, 1 (2006).
[57] Y. Ayyad *et al.*, Phys. Rev. C **91**, 034601 (2015).
[58] F. Méot, Nucl. Instrum. Methods Phys. Res., Sect. A **767**, 112 (2014).
[59] [http://geant4.cern.ch/].
[60] C. Scheidenberger *et al.*, Nucl. Instrum. Methods Phys. Res., Sect. B **142**, 441 (1998).
[61] A. Boudard, J. Cugnon, J. C. David, S. Leray, and D. Mancusi, Phys. Rev. C **87**, 014606 (2013).
[62] A. Kelić, M. V. Ricciardi, and K. H. Schmidt, in *Proceedings of Joint ICTP-IAEA Advanced Workshop on Model Codes for Spallation Reactions*, ICTP Trieste, Italy, 4–8 February 2008, edited by D. Filges, S. Leray, Y. Yariv, A. Mengoni, A. Stanculescu, and G. Mank (IAEA INDC(NDS)-530, Vienna, 2008), pp. 181–221.
[63] V. F. Weisskopf and P. H. Ewing, Phys. Rev. **57**, 472 (1940).
[64] A. Ya. Rusanov, M. G. Itkis, and V. N. Okolovic, Phys. At. Nucl. **60**, 683 (1997).
[65] P. Armbruster, Nucl. Phys. A **140**, 385 (1970).
[66] C. R. Morton *et al.*, Phys. Rev. C **52**, 243 (1995).
[67] P. N. Nadtochy, G. D. Adeev, and A. V. Karpov, Phys. Rev. C **65**, 064615 (2002).
[68] J. Randrup and P. Möller, Phys. Rev. C **88**, 064606 (2013).
[69] K. H. Schmidt *et al.*, Phys. Rev. C **87**, 034601 (2013).
[70] E. Hagebø and T. Lund, J. Inorg. Nucl. Chem. **37**, 1569 (1975).
[71] T. Enqvist *et al.*, Nucl. Phys. A **703**, 435 (2002).
[72] M. G. Itkis, V. N. Okolovich, A. Ya. Rusanov, and G. N. Smirenkin, Sov. J. Part. Nucl. **19**, 301 (1988).
[73] B. D. Wilkins, E. P. Steinberg, and R. R. Chasman, Phys. Rev. C **14**, 1832 (1976).
[74] F. Gönnenwein and B. Börsig, Nucl. Phys. A **530**, 27 (1991).
[75] I. Companis, M. Mirea, and A. Isbasescu, Rom. J. Phys. **56**, 63 (2011).
[76] C. Böckstiegel, S. Steinhäuser, K. H. Schmidt, H. G. Clerc, A. Grewe, A. Heinz, M. de Jong, A. R. Junghans, J. Müller, and B. Voss, Nucl. Phys. A **802**, 12 (2008).